ACS Biomaterials SCIENCE & ENGINEERING

pubs.acs.org/journal/abseba Article

# In Situ Visualization of Ferritin Biomineralization via Graphene Liquid Cell-Transmission Electron Microscopy

Surya Narayanan, Reza Shahbazian-Yassar,* and Tolou Shokuhfar*

Cite This: *ACS Biomater. Sci. Eng.* 2020, 6, 3208–3216 Read Online



**ABSTRACT:** Ferritin biomineralization is essential to regulate the toxic $Fe^{2+}$ iron ions in the human body. Unravelling the mechanism of biomineralization in ferritin facilitates our understanding of the causes underlying many iron disorder-related diseases. Until now, no report of in situ visualization of ferritin biomineralization events at nanoscale exists due to the requirement for high-resolution imaging of nanometer-sized ferritin proteins in their hydrated states. Herein, for the first time, we show that the biomineralization processes within individual ferritin proteins can be visualized by means of graphene liquid cell-transmission electron microscopy (GLC-TEM). The increase in the ratio of $Fe^{3+}/Fe^{2+}$ ions over time monitored via electron energy loss spectroscopy (EELS) reveals the change in oxidation state of iron oxide phases with time. This study lays a foundation for future investigations on iron regulation mechanisms in healthy and dysfunctional ferritins.

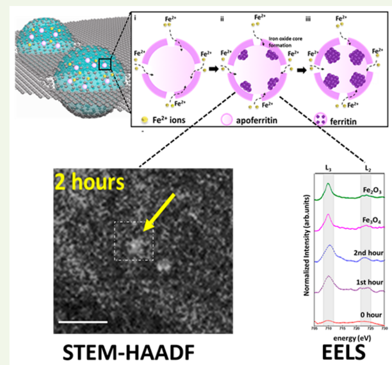


**KEYWORDS:** *ferritin proteins, biomineralization, in situ transmission electron microscopy, electron energy loss spectroscopy, graphene liquid cell*



## ■ INTRODUCTION

Many organisms exhibit a tendency to accumulate minerals to serve structural and metabolic functions in the human body.[1] The biominerals formed through the biologically controlled processes (also termed as biomineralization) exhibit unique structural and chemical properties different from abiotic mineralization.[1,2] Iron oxide mineralization in ferritin proteins is particularly interesting because of their role in iron regulation and storage. Further, the process of biomineralization in ferritin has implications in certain iron-related diseases in which iron accumulation is witnessed.[3−8] Iron biomineralization in ferritin also finds its application in biomimetics, wherein the primary focus is to synthesize iron oxide nanomaterials with defined size and crystallinity.[9]

The complexity in structure and the small size of ferritin proteins pose major limitations in understanding the storage mechanisms in real time.[10] There have been some efforts to monitor the biomineralization of ferritins with ex situ techniques,[11−17] such as UV visible spectroscopy, NMR spectroscopy, and Mossbauer spectroscopy, wherein the biomineralization was indicated by the changes in the physical phenomena, such as absorption of light or the emission of electromagnetic signals. However, these investigations lack spatial and chemical resolutions to observe the formation of iron oxide cores in individual ferritins in real time.[10] Consequently, these ex situ measurements were based on the cumulative results from several ferritin proteins. Considering these factors, it would be ideal to probe the individual proteins and observe the process of iron core formation.

The unique ability of transmission electron microscopy (TEM) to image and chemically probe nanoscale phenomenon in real time can facilitate new frontiers in biomineralization science. However, with conventional sample preparation techniques that can introduce artifacts,[18] it is impossible to image the biomineralization processes in real time. A time-resolved cryo-electron microscopy (CryoEM) can facilitate the visualization of the nucleation steps; however, freezing water might have implications in the protein density causing protein destabilization.[19] Also, the electron dose threshold for CryoEM imaging is quite low[20−22] to preserve the structural features of the protein, which this results in low signal-to-noise (SNR) ratio during imaging.

In situ liquid-cell TEM has recently emerged as a powerful method to study the dynamic interactions of materials in liquid solutions.[23,24] Several liquid-cell TEM studies based on microfluidic $Si_3N_4$ devices,[25−29] and graphene liquid cells (GLCs)[20,30−38] demonstrated the potential of this methodology to study biological materials in their native state. The studies of in situ iron-oxide biomineralization in magnetosome indicated the presence of magnetite with traces of hematite.[30]

**Received:** December 22, 2019
**Accepted:** April 13, 2020
**Published:** April 13, 2020

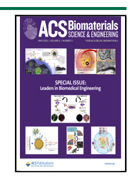

 

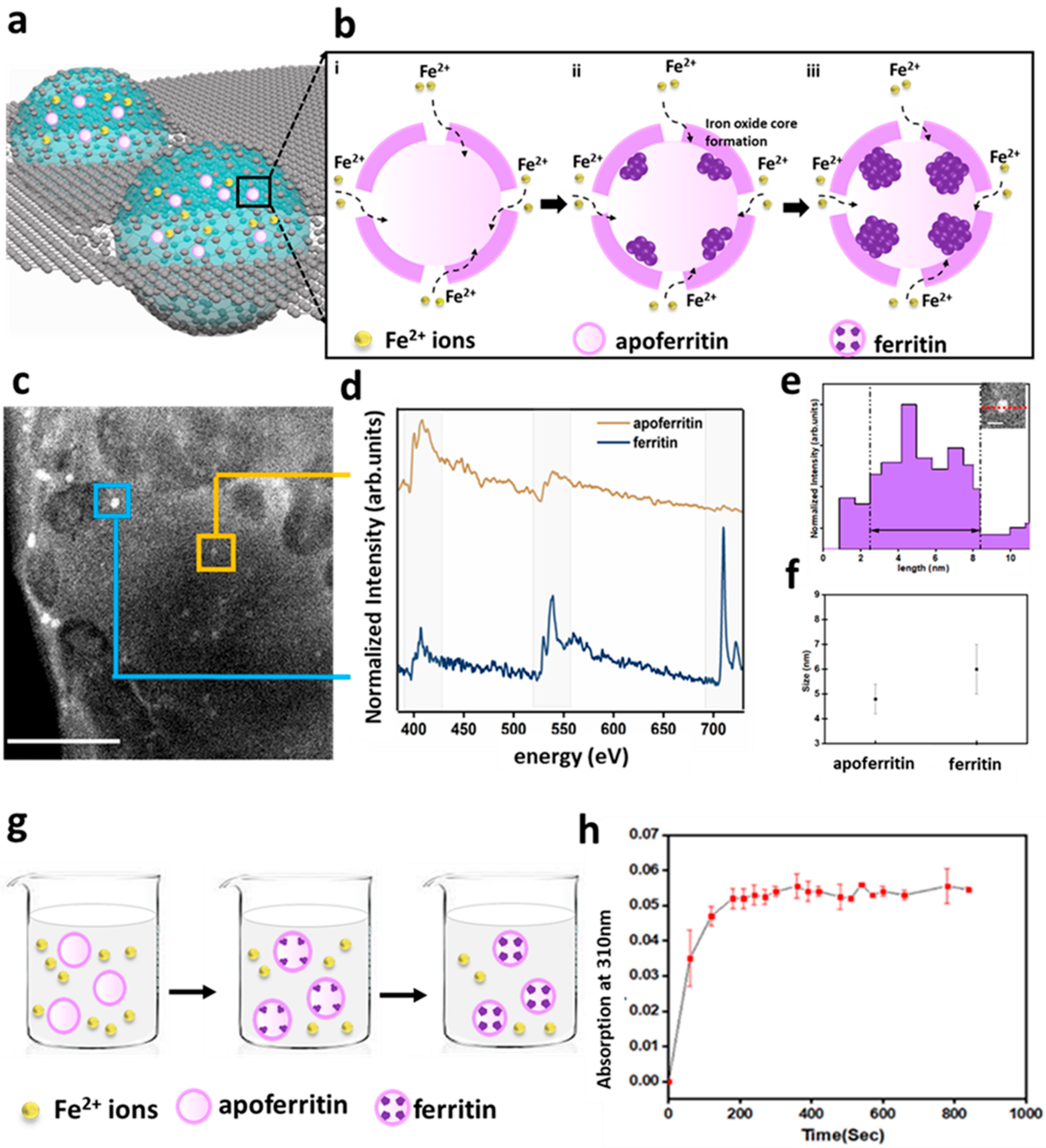


**Figure 1.** GLC as a chemical reactor where the biomineralization reaction is triggered. (a) Schematic representation of the GLC containing apoferritin (protein without iron) in iron rich environment. (b) Closer view of an apoferritin (b-i) wherein the reaction is triggered as the $Fe^{2+}$ ions in the solution enter the apoferritin (purple color shell). (b-ii) $Fe^{2+}$ ions oxidize and nucleate to form iron oxides core (violet color). (b-iii) New incoming $Fe^{2+}$ ions oxidize on the surface of already formed crystals facilitating the iron core growth. (c) HAADF image of mixture of apoferritin and ferritin present in GLC. The scale bar is 100 nm. (d) EELS data obtained from apoferritin and ferritin with the nitrogen (N), oxygen (O), and the iron (Fe) edge at 401, 532, and 701 eV, respectively. While apoferritin exhibits N and O signal, with no iron (Fe) signal, ferritin shows the presence of iron ions due the presence of Fe edge at 701 eV. (e) Line profile analysis of a ferritin protein obtained by drawing a line across the HAADF-STEM image of the protein core as shown in the inset. The scale bar in the HAADF-STEM image is 5 nm. The diameter of the protein core was determined by measuring the protein intensity with respect to background. (f) Size comparison of ferritin and apoferritin indicates that ferritin ($6 \pm 1$ nm) is slightly larger than apoferritin ($4.8 \pm 0.6$ nm) ($n = 30$). (g) Schematic depicts the ex situ biomineralization study in this work. Iron ions ($Fe^{2+}$) enters apoferritin to form ferritin with inner iron oxide core during biomineralization. (h) UV visible spectroscopy data show the change in absorbance with time. The oxidation of $Fe^{2+}$ ions to form $Fe^{3+}$ ions inside the protein, and the formation of diferric peroxidase intermediate results in the increase in absorbance of the solution with time.

Likewise, studies on mms6 proteins in microfluidic $Si_3N_4$ devices showed the self-assembly of protein and the iron binding on the surface of micelles can lower the energy barrier involved in the nucleation process.[39] However, these studies were limited in spatial resolution due to thick liquid and $Si_3N_4$ membranes and no chemical signature of biomineralization was reported.[40,41]

Here, for the first time, we investigated the iron biomineralization in ferritin in real-time using GLC-TEM technique (Figure 1). Because of the much lower thickness of


https://dx.doi.org/10.1021/acsbiomaterials.9b01889
ACS Biomater. Sci. Eng. 2020, 6, 3208−3216

graphene in comparison to $Si_3N_4$ membranes, the imaging and spectroscopic analysis could be conducted at high spatial and energy resolutions[35,42−45] In addition, the unique capability of graphene to scavenge the radiolysis species[37] is advantageous to study protein dynamics even with higher electron dose threshold than CryoEM. The method of using GLC-TEM to visualize small proteins is a major advance for studying biological materials in their hydrated state. In fact, this work builds upon our previous studies on utilization of GLC-TEM to study the morphology and chemistry of iron oxide cores in horse spleen, human spleen, and human heart ferritins.[32,33] While our earlier study[32] focused on morphological characterization of ferritin cores in hydrated states to determine the stable phases in human heart and human spleen ferritins, the present work reports direct observation of mineral growth in ferritin core (rather kinetic study). In this study, time-resolved high angle annular dark field (HAADF) imaging in scanning transmission electron microscopy (STEM) along with electron energy loss spectroscopy (EELS) were utilized to monitor the structural and chemical compositional changes in the iron core during ferritin biomineralization.

## ■ MATERIALS AND METHODS

**Materials Required for In Situ and Ex Situ Biomineralization.** Equine spleen apoferritin (ESaF) (0.2 $\mu$m filtered) (catalog no. A3641) was obtained from Sigma-Aldrich, USA. 3-*N*-(Morpholino)-propanesulfonic acid (MOPS) (catalog no. M1254), and ammonium iron(II) sulfate hexahydrate (catalog no. F1543) were purchased from Sigma-Aldrich, USA. The aqueous chemical solutions in this study were prepared using molecular biology reagent water (catalog no. W4502, Sigma-Aldrich). Aqueous solution of MOPS buffer (0.05 M) was prepared and the pH was adjusted to 7.5 with NaOH. Iron solution was prepared by dissolving 10 mM of Fe $(NH_4)_2$ $(SO_4)_2 \cdot 6H_2O$ in 1 mM HCl solution.

**Ex Situ Studies to Determine the Iron Biomineralization in Ferritin.** ESaF (0.3 $\mu$M) was added to 2 mL of MOPS buffered solution to maintain the pH as well as facilitate the iron uptake process. Further, 50 $\mu$L of freshly prepared iron solution was added to the apoferritin-buffered solution (800 iron ions/apoferritin). The absorbance was measured at 310 nm using UV−visible spectroscopy.

**In Situ GLC-TEM to Observe Ferritin Biomineralization in Real Time.** *TEM Sample Preparation.* For ferritin and apoferritin standards, a mixture of 0.15 $\mu$M of ferritin and apoferritin were mixed in the ratios of 1:1. Then, 1.5 $\mu$L of the mixture was used to make graphene sandwiches. For biomineralization experiment, 2 $\mu$L of the reaction mixture was pipetted after the addition of iron to the apoferritin-buffered solution. The drawn liquid was placed between two graphene (graphene supermarket, catalog no. SKU-TEM-CLC-025) coated lacey grids to form graphene sandwiches.

*Sample Characterization.* HAADF-STEM images were collected via the aberration corrected JEOL-JEM 200CF operated at 80 keV. The microscope is equipped with cold-field emission gun that can resolve materials with spatial resolution of 1.3 Å. A convergence semi angle of 22 and 17.8 mrad was used for STEM and EELS, respectively. The inner detection angle was set at 90 mrad for HAADF detector, to collect STEM images with better Z-contrast. A pixel size of 256 × 256 and dwell time of 31.2 $\mu$s were used to collect STEM images. On the other hand, 53.4 mrad was used for better quality EELS signal. The pixel size used during EELS imaging was 2.5 × 2.5 nm. The energy resolution for EELS was found to 1.5 eV (fwhm). The spectrum was acquired with the dispersion of 0.4 eV with pixel dwell time of 1 s to capture nitrogen, oxygen, and iron signal. A GLC area was defined at very low magnification (500k×) to prevent bubble formation or electron induced radiolysis. The probe step size used for the experiment was approximately 3 nm. Further, the beam was blocked after every reading to prevent electron induced biomineralization. The total electron dose for HAADF STEM image and EELS spectrum is approximately 7 and $10^4$ e/Å$^2$, respectively.

*Data Analysis.* The size and the intensity change in the proteins were observed via the line profile analysis from HAADF-STEM image. The line profile analysis is available in the digital micrograph software. EELS was utilized to observe the chemical changes in the protein. The signal from the EELS spectrum was first subtracted for its background, using digital micrograph software. A standard of 50 eV integration window was used as a background. Further energy ranges were considered from 380 to 730 eV to plot the nitrogen, oxygen, and iron peaks simultaneously. Further, an energy range of 705−730 eV was considered to understand the oxidation state of iron oxide during different stages of biomineralization. A graph was plotted against standard iron oxides to draw a comparison of ratios. The plot is representative of the iron signal after 3 channel spectrum averaging. To determine the ratio of $Fe^{3+}/Fe^{2+}$, the $L_3$ and the $L_2$ edge of iron peak was normalized and subtracted for any plural scattering Further, the area integral ratio was calculated by measuring the area under the Gaussian fit. The analysis was carried out using Origin Pro (version b9.4.0.220).[46]

## ■ RESULTS AND DISCUSSION

Figure 1 represents the schematic of our GLC approach to observe biomineralization in ferritins. Figure 1a is a graphene-based chemical reactor where the apoferritins (ferritins without iron) in the iron rich environment (Figure 1b-i) transform to ferritin due to the occurrence of iron oxide nucleation within the protein shell (Figure 1b-ii). The iron rich environment can further lead to the iron core growth in ferritin as shown in Figure 1b-iii. In the next step, HAADF-STEM imaging and EELS were conducted to differentiate apoferritins and ferritins in a solution. To this end, a mixture of 1:1 molar concentrations of ferritin and apoferritin was encapsulated in GLC. The yellow and blue box regions in Figure 1c indicates the existence higher image signal intensity in ferritin in comparison to apoferritin. This is expected considering that the HAADF image is particularly sensitive to the atomic number of the element[47] according to the relationship $I \alpha t. Z^2$, whereby, $I$ represents the intensity of electrons scattered, $t$ is the thickness of the iron oxide core, and $Z$ is the atomic number of the element. The contrast difference in the HAADF image supported the presence of higher atomic element (iron oxide) in ferritin, which was further verified by EELS (Figure 1d). The presence of iron peak at 701 eV in addition to the nitrogen and oxygen peak at 401 and 532 eV differentiates ferritin from apoferritin. In addition to the change in the contrast and the chemical signatures, a slight difference in the size was observed between apoferritin and ferritin as shown in Figure 1e and 1f. The difference in the size was analyzed by the line profile analysis as shown for one ferritin in Figure 1(e). Figure 1(f) indicates the difference in the average size of ferritin and apoferritin proteins (total of 30 ferritin and 30 apoferritin proteins were analyzed). It was observed that the size of apoferritin was approximately 4.8 ± 0.6 nm while the size of ferritin was 6 ± 1 nm. A significant change in the size of the core can be an indicative of varying size of iron oxide particles formed during biomineralization of ferritins as also indicated in previous studies.[32,48−50] While it is challenging to observe the protein shell without straining, the intensity of the HAADF image obtained from apoferritin could be due to the residual iron present inside the apoferritin.[51] The change in the size could represent the growth of iron nuclei within ferritin with time.

The changes in the appearance and the chemistry of the two proteins substantiated the fact that it might be possible to

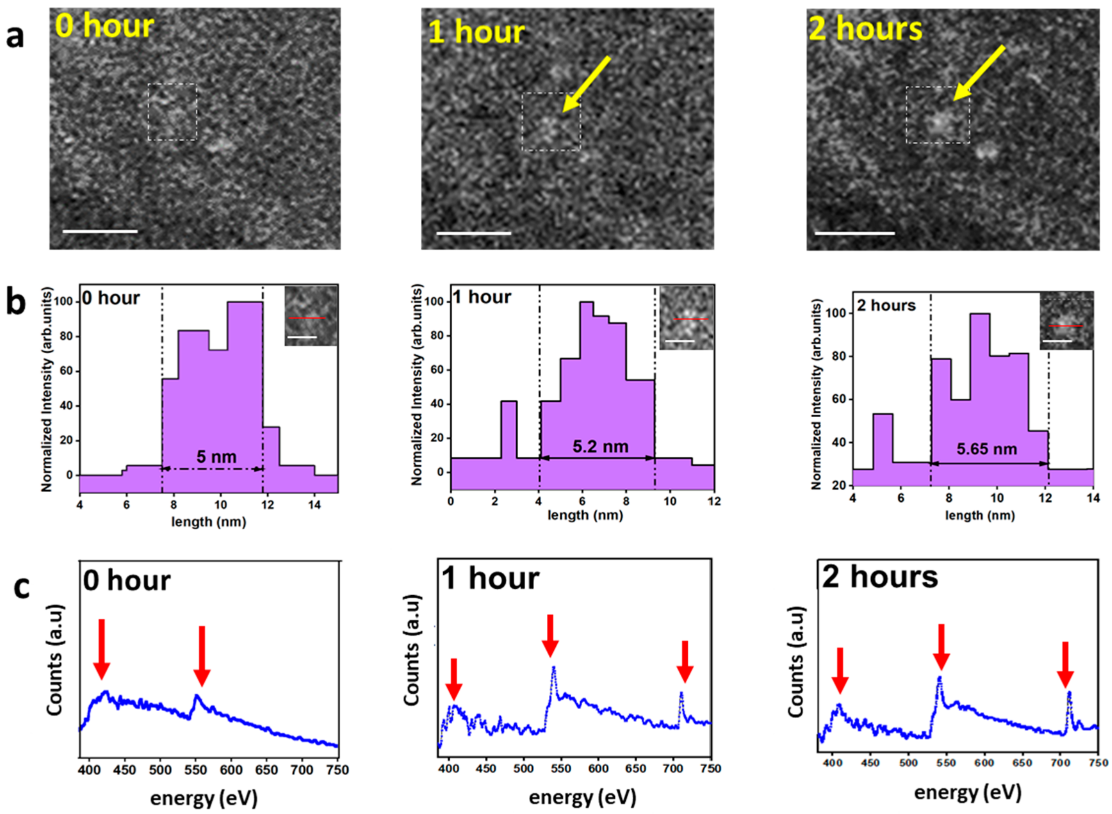


**Figure 2.** In situ biomineralization in ferritin via GLC-TEM: (a) HAADF-STEM image depicting the iron oxide core in ferritin during biomineralization at 0, 1, and 2 h. The white color square indicates the area of interest where the biomineralization is observed. The change in the contrast and the appearance of two ferritins proteins at the second hour (also indicated by the yellow color arrow) shows the formation of iron oxide core during biomineralization. Scale bar of the HAADF-STEM images are 50 nm. (b) Line-profile analysis indicates the change in the size of the core at different hours during biomineralization measured as 5 nm at the 0 h, 5.2 nm at the 1st hour, and 5.6 nm at the 2nd hour. The insets in the figures indicate the line drawn across the core. The scale bar of the image is 5 nm. The size is measured based on the change in the image intensity of the core with respect to the background. (c) EELS spectrum indicating the formation of nitrogen (401 eV) and oxygen (532 eV) at 0-h. The observation of additional iron $L_{23}$ edge (702 eV) at 1st and 2nd hour from the same protein indicating the phenomenon of biomineralization in the protein. The corresponding EELS spectrum was acquired from the area indicated by white color square in the HAADF images.

observe the biomineralization in real time. However, to be able to artificially mimic the iron rich environment and trigger the biomineralization reaction in GLC-TEM, it was important to optimize the physical and chemical conditions. To this end, ex situ experiments were executed to initiate the biomineralization reaction synthetically, as demonstrated by Snow et al.[52] (see Supporting Information for detailed procedure). Figure 1g depicts the schematic representation of the ex situ biomineralization reaction, wherein the biomineralization reaction is triggered by the addition of $Fe^{2+}$ ions in the apoferritin solution. The presence of MOPS buffer at a pH of 7.5 facilitates iron loading in the protein, thus converting apoferritin to ferritin.[52] This conversion of apoferritin to ferritin was confirmed by observing the visible change in the absorbance via UV visible spectroscopy (Figure 1h). Since, it was suggested that the absorbance for iron biomineralization is stronger at 310 nm,[52] we observed the changes in the absorbance at this range of wavelength. The curve formed is a representative of the iron biomineralization reaction involving MOPS buffer, which is well studied in the literature.[11,53−55] The $Fe^{2+}$ ions that enter the apoferritin shell forms peroxide complex in absence of ferroxidase center (<15% H subunits in equine spleen ferritin). The reaction further becomes catalytic when the $Fe^{2+}$ ions (bound to glutamate) reacts with dioxygen, thus attracting and oxidizing the incoming iron ions.[11] Eventually, once the core is formed, the additional $Fe^{2+}$ ions that enters the protein oxidizes on the surface of the core, resulting in reactions reaching a plateau.[52] It is shown that the crystal continues to grow until the protein is at least half-full of minerals.[55] It should be noted that our ex situ results demonstrate the feasibility of iron biomineralization through artificial means and does not show the activity within the protein after 2 h. While the MOPS buffer can be replaced by several different buffers to trigger ex situ biomineralization reactions in ferritin,[56] the reaction mechanism is different for each buffer. MOPS buffer was used in this study since it is a widely used buffer to trigger biomineralization reaction in ferritin.[11,12,15,57−59]

Figure 2 depicts the time-resolved iron core formation in individual ferritins via the GLC-TEM. Figure 2a represents the HAADF-STEM images of biomineralization in apoferritins at different time frames (0, 1, and 2 h). The white color square represents the area of interest that features a protein in which biomineralization was observed. On the basis of the earlier observation of contrast difference between apoferritin and ferritin (Figure 1c), apoferritins were identified as proteins with lower image intensity compared to ferritins. This is also observed at the 0 h in Figure 2a as the protein within the white square area of interest appears as faint compared to the adjacent protein in the same area which is a biomineralized


https://dx.doi.org/10.1021/acsbiomaterials.9b01889
ACS Biomater. Sci. Eng. 2020, 6, 3208−3216

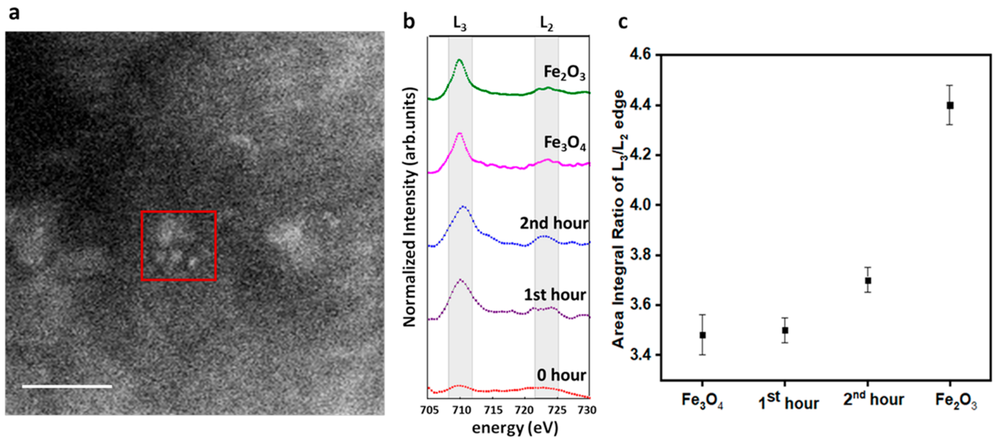


**Figure 3.** In situ chemical characterization of apoferritin biomineralization in GLC-STEM. (a) HAADF image representing an area within GLC in which ferritin proteins undergo biomineralization. The red square represents the region of interest from where the EELS data were acquired (Scale bar is 100 nm). (b) EELS data showing the Fe $L_2$ and $L_3$ edges of iron oxides obtained during biomineralization. The Fe $L_2$ and $L_3$ edges are compared with the iron oxide standards ($Fe_3O_4$ and $Fe_2O_3$) to identify the composition of iron oxide. (c) Area integral ratios of $L_3/L_2$ of Fe edge plotted to determine the iron oxidation states during mineralization. The standard errors represent the errors in the fitting of the Gaussian curves beneath the $L_3$ and $L_2$ peaks.

ferritin. As the reaction progressed, there was a change in the contrast of the protein (indicated by yellow color arrow) at the first and second hour compared to the 0 h. The addition of iron ions within the protein contributes to the contrast change observed during biomineralization which was also studied earlier in the literature.[60,48] The increase in the number of iron ions was also supported by the line profile analysis which indicated the variation in the diameter of the core during biomineralization (Figure 2b). The length was a measure of difference in the image intensity of the core with respect to background as shown in the insets of Figure 2b). The size of the core increased from 4.2 ± 0.3 nm at 0 h to 4.9 ± 0.3 nm at 1 h and eventually to 5.1 ± 0.3 nm after 2 h ($n$ = 5) (Figure S1). It would be interesting to measure the number of iron ions that enter the core of the proteins to determine the core formation and observing the oxidation of additional $Fe^{2+}$ ions on the surface of the core when they enter the protein. The beam was blanked after every data acquisition to prevent electron dose induced biomineralization. The total electron dose was $10^4$ electrons/Å$^2$ with pixel dwell time of 0.5 s. This experiment was also repeated, and consistent observation was made. As an example, Figure S2 is another evidence showing the change in the intensity of iron oxide core within ferritin proteins with time during biomineralization. While the increase in the size of the protein core can indicate the progress of biomineralization, it should be noted that it is challenging to obtain consistent size change among several proteins in GLCs. Factors, such as concentration of iron ions surrounding the protein, and the volume of GLCs might influence the kinetics of biomineralization. Although, it is possible to study these aspects by including large data sets, the process and observation made is localized to a specific TEM area. Hence, it is challenging to collect large data sets. Future studies should focus on the design aspects to control the biomineralization kinetics as well as to observe these processes simultaneously in different areas of the TEM grids.

Further, to substantiate the fact that the change observed in the HAADF STEM image is due to biomineralization in proteins, chemical analysis was performed via time-resolved EELS. Figure 2c represents the chemical analysis of the protein undergoing biomineralization. At 0 h, which is also the onset of biomineralization, apoferritins were imaged. It is expected that the iron core formation inside the protein is not initiated at this stage. This is also supported by the EELS data, which shows the nitrogen, and the oxygen signal from the protein. However, there are no traces of iron at this stage evident by the lack of iron signal at 702 eV. Mossbauer spectroscopy[61] and resonance Raman spectroscopy[62] studies suggests that it takes 12−24 h to complete the biomineralization process in ferritin.[63] However, during biomineralization, it is expected that the iron ions enter the protein shell to form iron oxide core inside the protein. This is reflected by the iron signal in addition to nitrogen and oxygen signals in EELS at the first hour after the onset of biomineralization. The presence of nitrogen signal substantiates the fact that iron biomineralization is observed inside the protein shell and not outside the protein. At the second hour after the onset of the reaction, the formation of iron oxides composites within the protein shell was evident. This was indicated by a significant difference in the SNR ratio of iron $L_{23}$ edge at the second hour, compared to the first hour after the start of the biomineralization reaction. The EELS data obtained in Figure 2c also supports the change in the contrast and size of the core as shown in Figure 2a and 2b. To ensure that the liquid around the protein remains intact during biomineralization, the low-loss peak was monitored simultaneously as shown in Figure S3. The observation of a peak at 9 eV indicated the presence of liquid around the protein (Figure S3). Further, additional experiments were also conducted to determine the quality of the liquid pockets after data collection during biomineralization (Figure S4). It was observed that the liquid in the GLCs remained intact even after EELS acquisition.

To understand the chemical composition of iron oxides formed during biomineralization, the iron $L_{23}$ edge obtained during different stages of biomineralization were collected and compared with the iron oxide standards. Figure 3a represents one such GLC-TEM area from which EELS of the iron $L_{23}$ edge was obtained (Figure 3b). The gray area in Figure 3b represents the $L_3$ and $L_2$ edges at 708 and 721 eV. While there are white lines observed at first and second hour suggesting the formation of iron oxide, the 0 h represents the absence of iron oxide indicated by the absence of white lines. To obtain the


https://dx.doi.org/10.1021/acsbiomaterials.9b01889
ACS Biomater. Sci. Eng. 2020, 6, 3208−3216

oxidation states, the area integral ratios of $L_3/L_2$ edge were calculated. It has been shown that by evaluating the integral area of $L_3/L_2$, the ratios of $Fe^{3+}/Fe^{2+}$ iron ions in the core can be determined.[64] The ratios of $L_3/L_2$ edge were compared with iron oxide standards to identify the kind of iron oxides formed with time. The ratios were compared with $Fe_3O_4$ standards ($L_3/L_2 = 3.5 \pm 0.1$) consisting of both $Fe^{2+}$ and $Fe^{3+}$ ions and $Fe_2O_3$ ($L_3/L_2 = 4.4 \pm 0.2$) standards made of $Fe^{3+}$ ions. These iron oxides standards were chosen based on our previous study on human ferritins in GLC, wherein we observed that the iron core composition is made of ferrihydrite, hematite, magnetite or maghemite.[18] While there are several naturally occurring phases of iron oxides, ferritin does not exhibit all the phases, rather the protein microenvironment influences the formation of specific iron oxide phases.[65] It was interesting to note that during the first hour of biomineralization, the ratio of $L_3/L_2$ ($3.5 \pm 0.08$) was comparable with the ratio of the oxidation states of $Fe_3O_4$ ($L_3/L_2 = 3.5 \pm 0.05$) (Figure 3c). However, with a progress in the reaction, there was an inclination in the slope as the ratios of $Fe^{3+}/Fe^{2+}$ increased to $3.7 \pm 0.05$ at the second hour. The ratios of $Fe^{3+}/Fe^{2+}$ at the second hour of biomineralization was an intermediate between the ratios of $Fe_3O_4$ and $Fe_2O_3$.

While there are several studies which report the observation of $Fe_3O_4$(magnetite)[66−69] and $Fe_2O_3 \cdot 0.5H_2O$-(ferrihydrite)[70,65,10,49] in ferritin, it should be noted that the earlier studies focused on imaging and characterization of fully biomineralized iron core in ferritin. There is only one study, thus far, that describes the iron oxide phase transformations during iron core removal.[69] On the basis of this study,[69] it was concluded that magnetite was observed as a dominant iron oxide phase in ferritins with less than 500 iron ions. However, with increase in the number of iron ions, a phase shift was observed and the proteins expressed high ratios of ferrihydrite.[69]

Although a similar trend is observed in our study, it is also important to consider the mechanism of iron oxidation in ferritin. A recent biochemical study showed that the L-amino acid subunits chain facilitate iron oxidation on the surface of the mineral core in addition to the oxidation at the ferroxidase sites.[59] This suggests a possibility that the iron nucleation and the iron core formation happen even before the proteins could be filled with iron ions. The iron ions that enter the protein might oxidize and nucleate spontaneously while the $Fe^{2+}$ ions might continue to enter the protein channels. Thus, there is a possibility of a mixed iron oxide phase ($Fe^{2+}$, $Fe^{3+}$) at the earlier stages of biomineralization as observed during the first hour after the onset of biomineralization (Figure 3c). However, the newly entered $Fe^{2+}$ ions might continue to oxidize on the surface of the core, which might have resulted in the increase in the ratios of $Fe^{3+}/Fe^{2+}$, which was observed at the second hour after the onset of biomineralization. It should be noted that Mehlenbacher et al.[59] produced heteropolymeric cages with different H/L ratios, while the current system explores the commercially available ferritin. While the discussion above suggests possibilities for the observational changes, future studies should draw a comparison between ferritins obtained from the same source.

Although dose rates were employed to collect the EELS spectrum data from each pixel across the protein core, total doses were employed to study the effect of electron beam radiation on the iron core of the whole protein. Thus, to understand the effect of electron dose on the protein core, we studied the iron oxide transformations in ferritin via GLC-TEM. The ferritins encapsulated in GLCs were subjected to different cumulative electron dose as shown in Figure 4. Since

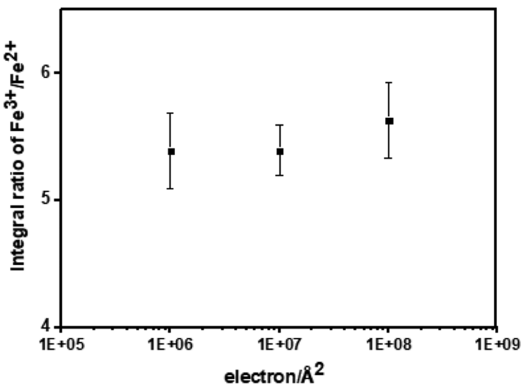


**Figure 4.** Cumulative electron dose in STEM to evaluate the changes in integral area ratios of $Fe^{3+}/Fe^{2+}$ iron ions in ferritin encapsulated within GLC ($n = 3$).

the integral ratios of $L_3$ to $L_2$ edge were considered to determine the oxidation state of iron in ferritin, this study also evaluated the electron dose with respect to the integral ratios of iron $L_{23}$ edge. It was observed that the ratios of $Fe^{3+}/Fe^{2+}$ remained the same despite varying the cumulative electron dose from $10^5$ to $10^8$ electrons/Å$^2$ (Figure 4). The range of the electron doses were chosen based on the earlier studies reported by Pan et al.,[49] who also studied ferritin in dry state at different electron doses. The electron dose reported in this study also falls within this range. The EELS plots of Figure 4 have been included in the Supporting Information (Figure S5). As mentioned above, the observation made in this study is similar to the results obtained by Pan et al.[49] They showed that the ratios of $Fe^{3+}/Fe^{2+}$ remained the same through different electron doses, although a change was observed in the $Fe^{3+}$ ions as they moved from octahedral to tetrahedral sites during electron induced damage.[49]

While our studies show that electron doses below $10^6$ electrons/Å$^2$ can prevent iron oxide transformations in GLC as also reported in the literature,[49,71,72] a recent study by Keskin and de Jonge[20] showed that the electron dose density for a biological material is much lower than traditional beam sensitive nanomaterials. It should be noted that ferritin is inherently made up of two different materials−protein shell and the iron oxide nanoparticles. While it was observed that the EELS should be collected at or below $10^6$ electron/ Å$^2$ to prevent electron induced iron oxide transformation of the iron oxide nanoparticles, it was observed that the stipulated dose was still high enough to prevent biomineralization in ferritin. Even though having lower electron dose rate can protect the integrity of proteins,[33] the most important aspect is defining the EELS probe step size, pixel dwell time, as well as the pixel size to be able to control the dose density. To mitigate the electron dose below $10^6$ electron/ Å$^2$, we under-sampled the region of interest while collecting the EELS. Further, larger STEM pixel size of $2.5 \times 2.5$ mm was used during EELS acquisition with the pixel dwell time of 0.5 s. As a result, the electron dose density could be controlled. One should also consider the SNR ratio when defining the pixel size and the probe step size. Often, the SNR is poor, when the probe step size is bigger, and the exposure time is minimized. This results


https://dx.doi.org/10.1021/acsbiomaterials.9b01889
ACS Biomater. Sci. Eng. 2020, 6, 3208−3216

in a poor-quality spectrum making it difficult to observe the changes in the composition. Hence, the experiments were repeated several times to optimize the EELS parameters to obtain enough resolution to study the changes (Figure S6). The experiments were further carefully controlled by blanking the beam after every reading to prevent electron dose history and its consequence in the biomineralization process.

Further, to evaluate whether the iron oxide formation in ferritin is occurring naturally or due to the consequence of exposed electron dose during EELS acquisition, the biomineralization experiments were carried out without prior electron beam exposure, and the chemical composition of the biomineralized ferritin was analyzed after 2 h of the experiment. Figure S7 represents the GLC-TEM image of the control group (apoferritins) and the iron core formed in ferritin at 2 h of biomineralization without prior exposure to electron dose. The integral ratio of $Fe^{3+}/Fe^{2+}$ was calculated and found out the value to be $3.9 \pm 0.1$. The ratio of $Fe^{3+}/Fe^{2+}$ obtained through this study was comparable with the ratios of $Fe^{3+}/Fe^{2+}$ obtained in the in situ experiment.

The observed iron oxide minerals formed at the second hour of biomineralization was not comparable to a fully grown iron oxide crystal in ferritin. Further, the ratios obtained at the second hour was not close to the ratios of $Fe_2O_3$. To observe the changes and see the fully grown crystals, the experiment was continued for several hours. However, there was no change observed in the biomineralization process after the second hour. While the presence of liquid was observed in the sample after 2 h, there is a possibility of electron dose irradiation after several EELS acquisition.[73] Although dose rates employed in this study were below the threshold dose rates, there is an accumulated total electron dose when the same area is exposed to electron dose during each data acquisition. While it is possible to monitor the effect of total dose on the protein core (as in Figure 4), it is challenging to evaluate the physical changes in the surrounding liquid that might possibly occur due to the electron dose history. With advancements in STEM-EELS, such as the utilization of modern direct detectors,[74] it might be possible to obtain qualitative EELS spectrum data with better SNR while maintaining the low electron dose density. Future studies should also include the possibilities of thermodynamics driven iron oxide phase transformations in liquid under the influence of electron beam.

## ■ CONCLUSION

In summary, we visualized the in situ iron internalization process in ferritin proteins, for the first time, by utilizing GLC-TEM. The proteins were visible without heavy metal staining. Further, we could witness a contrast change in the HAADF STEM image because of the iron loading inside the protein. The evidence from this study suggests that GLC-TEM can be utilized to study biological reactions in real time. On the basis of the time-resolved EELS, it was possible to observe the chemical compositional change in a single protein in real-time while mitigating the effect of electron dose. The iron ions encapsulated in the GLC triggered the formation of iron oxide core inside apoferritin (protein without iron) through the process of biomineralization. Through time-resolved EELS, it was observed that the iron core at the first hour after the onset of biomineralization expressed chemical components of mixed valence state. However, the composition of the protein leaned toward higher ratios of $Fe^{3+}/Fe^{2+}$ at the second hour of biomineralization. The iron ions presence, the mechanism of iron oxidation, and the thermodynamic factors at the nanoscale might influence the formation of specific iron oxide phases. Due to electron beam sensitivity, our in situ TEM observations were confined to 2 h. Future studies should focus on utilizing high speed and low dose EELS, which can also provide better SNR to identify the differences in the composition of the mineral phases. It would be interesting to study the differences in the oxidation kinetics of ferritin with varying heavy subunit chain (H−)/light subunit chain (L−) ratios. Studies should also focus on confinement effects of the GLCs and its contribution toward the kinetics of biomineralization. Future studies can also focus on comparing the results obtained through the GLC technique with other techniques, such as X-ray crystallography.[11]

## ■ ASSOCIATED CONTENT

### Supporting Information

The Supporting Information is available free of charge at https://pubs.acs.org/doi/10.1021/acsbiomaterials.9b01889.

Experimental methods, mechanism of biomineralization, and all the control experiments (PDF)

## ■ AUTHOR INFORMATION


### Corresponding Authors

**Reza Shahbazian-Yassar** − *Department of Mechanical and Industrial Engineering, University of Illinois at Chicago, Chicago, Illinois 60607, United States;* orcid.org/0000-0002-7744-4780; Email: rsyassar@uic.edu

**Tolou Shokuhfar** − *Department of Bioengineering, University of Illinois at Chicago, Chicago, Illinois 60607, United States;* orcid.org/0000-0002-7905-2748; Email: tolou@uic.edu

### Author

**Surya Narayanan** − *Department of Bioengineering, University of Illinois at Chicago, Chicago, Illinois 60607, United States*

Complete contact information is available at: https://pubs.acs.org/10.1021/acsbiomaterials.9b01889


### Author Contributions

S.N. performed the experiments and wrote the manuscript. R.S.-Y. and T.S. contributed to the discussion and editing of the manuscript.

### Notes

The authors declare no competing financial interest.

## ■ ACKNOWLEDGMENTS

This work is funded by National Science Foundation CAREER award (DMR-1564950). R.S.-Y.'s contribution is supported by NSF DMR-1710049. The authors would like to acknowledge Nasim Farajpour for the schematic image. This work made use of instruments in the Electron Microscopy Core of UIC's Research Resources Centre. The UIC JEOL JEM-ARM200CF is supported by an MRI-R2 grant from the National Science Foundation (Grant No. DMR-0959470). The authors acknowledge UIC Research Resource Centre for providing the instrumental support.

## ■ REFERENCES

(1) Weiner, S. An Overview of Biomineralization Processes and the Problem of the Vital Effect. *Rev. Mineral. Geochem.* **2003**, *54* (1), 1−29.

(2) Chen, Y.; Feng, Y.; Deveaux, J. G.; Masoud, M. A.; Chandra, F. S.; Chen, H.; Zhang, D.; Feng, L. Biomineralization Forming Process and Bio-Inspired Nanomaterials for Biomedical Application: A Review. *Minerals* **2019**, 68.

(3) Levi, S.; Finazzi, D. Neurodegeneration with Brain Iron Accumulation: Update on Pathogenic Mechanisms. *Front. Pharmacol.* **2014**, *5*, 99.

(4) Chen, J.; Marks, E.; Lai, B.; Zhang, Z.; Duce, J. A.; Lam, L. Q.; Volitakis, I.; Bush, A. I.; Hersch, S.; Fox, J. H. Iron Accumulates in Huntington's Disease Neurons: Protection by Deferoxamine. *PLoS One* **2013**, *8* (10), e77023.

(5) Rouault, T. A. Iron Metabolism in the CNS: Implications for Neurodegenerative Diseases. *Nature Reviews Neuroscience* **2013**, 551−564, DOI: 10.1038/nrn3453.

(6) Quintana, C.; Gutiérrez, L. Could a Dysfunction of Ferritin Be a Determinant Factor in the Aetiology of Some Neurodegenerative Diseases? *Biochim. Biophys. Acta, Gen. Subj.* **2010**, *1800*, 770−782.

(7) Gujja, P.; Rosing, D. R.; Tripodi, D. J.; Shizukuda, Y. Iron Overload Cardiomyopathy: Better Understanding of an Increasing Disorder. *Journal of the American College of Cardiology* **2010**, 1001−1012, DOI: 10.1016/j.jacc.2010.03.083.

(8) Telfer, P. T.; Prestcott, E.; Holden, S.; Walker, M.; Hoffbrand, A. V.; Wonke, B. Hepatic Iron Concentration Combined with Long-Term Monitoring of Serum Ferritin to Predict Complications of Iron Overload in Thalassaemia Major. *Br. J. Haematol.* **2000**, *110* (4), 971−977.

(9) Jutz, G.; Van Rijn, P.; Santos Miranda, B.; Böker, A. Ferritin: A Versatile Building Block for Bionanotechnology. *Chem. Rev.* **2015**, *115* (4), 1653−1701.

(10) Theil, E. C.; Liu, X. S.; Matzapetakis, M. Ferritin. Biomineralization of Iron. *Biomineralization: From Nature to Application* **2010**, *4*, 327−341.

(11) Pozzi, C.; Ciambellotti, S.; Bernacchioni, C.; Di Pisa, F.; Mangani, S.; Turano, P. Chemistry at the Protein−Mineral Interface in L-Ferritin Assists the Assembly of a Functional (μ 3 -Oxo)Tris[(μ 2 -Peroxo)] Triiron(III) Cluster. *Proc. Natl. Acad. Sci. U. S. A.* **2017**, *114* (10), 2580−2585.

(12) Turano, P.; Lalli, D.; Felli, I. C.; Theil, E. C.; Bertini, I. NMR Reveals Pathway for Ferric Mineral Precursors to the Central Cavity of Ferritin. *Proc. Natl. Acad. Sci. U. S. A.* **2010**, *107*, 545−550.

(13) Papaefthymiou, G. C. The Mössbauer and Magnetic Properties of Ferritin Cores. *Biochimica et Biophysica Acta - General Subjects* **2010**, 886−897.

(14) Cho, K. J.; Shin, H. J.; Lee, J. H.; Kim, K. H. J.; Park, S. S. S. S.; Lee, Y.; Lee, C.; Park, S. S. S. S.; Kim, K. H. J. The Crystal Structure of Ferritin from Helicobacter Pylori Reveals Unusual Conformational Changes for Iron Uptake. *J. Mol. Biol.* **2009**, *390* (1), 83−98.

(15) Hwang, J.; Penner-Hahn, J. E.; et al. A Short Fe-Fe Distance in Peroxodiferric Ferritin: Control of Fe Substrate versus Cofactor Decay? *Science (Washington, DC, U. S.)* **2000**, *287* (5450), 122−125.

(16) Tian, L.; Cao, C.; Pan, Y. The Influence of Reaction Temperature on Biomineralization of Ferrihydrite Cores in Human H-Ferritin. *BioMetals* **2012**, *25* (1), 193−202.

(17) Bertini, I.; Lalli, D.; Mangani, S.; Pozzi, C.; Rosa, C.; Theil, E. C.; Turano, P. Structural Insights into the Ferroxidase Site of Ferritins from Higher Eukaryotes. *J. Am. Chem. Soc.* **2012**, *134* (14), 6169−6176.

(18) Narayanan, S.; Shahbazian-Yassar, R.; Shokuhfar, T. Transmission Electron Microscopy of the Iron-Oxide Core in Ferritin Proteins: Current Status and Future Directions. *J. Phys. D: Appl. Phys.* **2019**, *52* (45), 453001.

(19) Halle, B. Biomolecular Cryocrystallography: Structural Changes during Flash-Cooling. *Proc. Natl. Acad. Sci. U. S. A.* **2004**, *101* (14), 4793−4798.

(20) Keskin, S.; De Jonge, N. Reduced Radiation Damage in Transmission Electron Microscopy of Proteins in Graphene Liquid Cells. *Nano Lett.* **2018**, *18* (12), 7435−7440.

(21) Carlson, D. B.; Evans, J. E. Low-Dose Imaging Techniques for Transmission Electron Microscopy. *Transmission Electron Microscope* **2012**, 3−22.

(22) Dissanayake, T. U.; Wang, M.; Woehl, T. J. A Fluorescence Microscopy Assay for Assessing Beam Damage to Nanoparticle Capping Ligands During Liquid Cell Electron Microscopy. *Microsc. Microanal.* **2019**, *25* (S2), 1672−1673.

(23) de Jonge, N.; Ross, F. M. Electron Microscopy of Specimens in Liquid. *Nat. Nanotechnol.* **2011**, *6*, 695−704.

(24) Ross, F. M. Opportunities and Challenges in Liquid Cell Electron Microscopy. *Science (Washington, DC, U. S.)* **2015**, *350* (6267), aaa9886.

(25) Peckys, D. B.; De Jonge, N. Visualizing Gold Nanoparticle Uptake in Live Cells with Liquid Scanning Transmission Electron Microscopy. *Nano Lett.* **2011**, *11* (4), 1733−1738.

(26) Murai, T.; Maruyama, Y.; Mio, K.; Nishiyama, H.; Suga, M.; Sato, C. Low Cholesterol Triggers Membrane Microdomain-Dependent CD44 Shedding and Suppresses Tumor Cell Migration. *J. Biol. Chem.* **2011**, *286* (3), 1999−2007.

(27) Peckys, D. B.; Mazur, P.; Gould, K. L.; De Jonge, N. Fully Hydrated Yeast Cells Imaged with Electron Microscopy. *Biophys. J.* **2011**, *100* (10), 2522−2529.

(28) Hoppe, S. M.; Sasaki, D. Y.; Kinghorn, A. N.; Hattar, K. In-Situ Transmission Electron Microscopy of Liposomes in an Aqueous Environment. *Langmuir* **2013**, *29* (32), 9958−9961.

(29) Kennedy, E.; Nelson, E. M.; Tanaka, T.; Damiano, J.; Timp, G. Live Bacterial Physiology Visualized with 5 Nm Resolution Using Scanning Transmission Electron Microscopy. *ACS Nano* **2016**, *10* (2), 2669−2677.

(30) Firlar, E.; Ouy, M.; Bogdanowicz, A.; Covnot, L.; Song, B.; Nadkarni, Y.; Shahbazian-Yassar, R.; Shokuhfar, T. Investigation of the Magnetosome Biomineralization in Magnetotactic Bacteria Using Graphene Liquid Cell-Transmission Electron Microscopy. *Nanoscale* **2019**, *11* (2), 698−705.

(31) Firlar, E.; Ouy, M.; Covnot, L.; Xing, Y.; Lee, D.; Chan, A.; He, Y.; Song, B.; Afelik, S.; Wang, Y.; Shahbazian-Yassar, R.; Oberholzer, J.; Shokuhfar, T. In Situ Graphene Liquid Cell-Transmission Electron Microscopy Study of Insulin Secretion in Pancreatic Islet Cells. *Int. J. Nanomed.* **2019**, *14*, 371−382.

(32) Narayanan, S.; Firlar, E.; Rasul, M. G.; Foroozan, T.; Farajpour, N.; Covnot, L.; Shahbazian-Yassar, R.; Shokuhfar, T. On the Structure and Chemistry of Iron Oxide Cores in Human Heart and Human Spleen Ferritins Using Graphene Liquid Cell Electron Microscopy. *Nanoscale* **2019**, *11*, 16868.

(33) Wang, C.; Qiao, Q.; Shokuhfar, T.; Klie, R. F. High-Resolution Electron Microscopy and Spectroscopy of Ferritin in Biocompatible Graphene Liquid Cells and Graphene Sandwiches. *Adv. Mater.* **2014**, *26* (21), 3410−3414.

(34) Wojcik, M.; Hauser, M.; Li, W.; Moon, S.; Xu, K. Graphene-Enabled Electron Microscopy and Correlated Super-Resolution Microscopy of Wet Cells. *Nat. Commun.* **2015**, *6* (1), 7384.

(35) Chen, Q.; Smith, J. M.; Park, J.; Kim, K.; Ho, D.; Rasool, H. I.; Zettl, A.; Alivisatos, A. P. 3D Motion of DNA-Au Nanoconjugates in Graphene Liquid Cell Electron Microscopy. *Nano Lett.* **2013**, *13* (9), 4556−4561.

(36) Park, J.; Park, H.; Ercius, P.; Pegoraro, A. F.; Xu, C.; Kim, J. W.; Han, S. H.; Weitz, D. A. Direct Observation of Wet Biological Samples by Graphene Liquid Cell Transmission Electron Microscopy. *Nano Lett.* **2015**, *15* (7), 4737−4744.

(37) Cho, H.; Jones, M. R.; Nguyen, S. C.; Hauwiller, M. R.; Zettl, A.; Alivisatos, A. P. The Use of Graphene and Its Derivatives for Liquid-Phase Transmission Electron Microscopy of Radiation-Sensitive Specimens. *Nano Lett.* **2017**, *17* (1), 414−420.

(38) Donovan, A. J.; Kalkowski, J.; Szymusiak, M.; Wang, C.; Smith, S. A.; Klie, R. F.; Morrissey, J. H.; Liu, Y. Artificial Dense Granules: A Procoagulant Liposomal Formulation Modeled after Platelet Polyphosphate Storage Pools. *Biomacromolecules* **2016**, *17* (8), 2572−2581.

(39) Kashyap, S.; Woehl, T. J.; Liu, X.; Mallapragada, S. K.; Prozorov, T. Nucleation of Iron Oxide Nanoparticles Mediated by Mms6 Protein in Situ. *ACS Nano* **2014**, *8* (9), 9097−9106.

(40) He, K.; Shokuhfar, T.; Shahbazian-Yassar, R. Imaging of Soft Materials Using in Situ Liquid-Cell Transmission Electron Microscopy. *J. Phys.: Condens. Matter* **2019**, *31* (10), 103001.

(41) Evans, J. E.; Jungjohann, K. L.; Wong, P. C. K.; Chiu, P. L.; Dutrow, G. H.; Arslan, I.; Browning, N. D. Visualizing Macromolecular Complexes with in Situ Liquid Scanning Transmission Electron Microscopy. *Micron* **2012**, *43* (11), 1085−1090.

(42) Ghodsi, S. M.; Megaridis, C. M.; Shahbazian-Yassar, R.; Shokuhfar, T. Advances in Graphene-Based Liquid Cell Electron Microscopy: Working Principles, Opportunities, and Challenges. *Small Methods* **2019**, *3*, 1900026.

(43) Yuk, J. M.; Park, J.; Ercius, P.; Kim, K.; Hellebusch, D. J.; Crommie, M. F.; Lee, J. Y.; Zettl, A.; Alivisatos, A. P. High-Resolution Em of Colloidal Nanocrystal Growth Using Graphene Liquid Cells. *Science (Washington, DC, U. S.)* **2012**, *336* (April), 61−64.

(44) Berry, V. Impermeability of Graphene and Its Applications. *Carbon* **2013**, *62*, 1−10.

(45) Ghodsi, S. M.; Anand, S.; Shahbazian-Yassar, R.; Shokuhfar, T.; Megaridis, C. M. In Situ Study of Molecular Structure of Water and Ice Entrapped in Graphene Nanovessels. *ACS Nano* **2019**, *13* (4), 4677−4685.

(46) Graetz, J.; Ahn, C. C.; Ouyang, H.; Rez, P.; Fultz, B. White Lines and D-Band Occupancy for the 3d Transition-Metal Oxides and Lithium Transition-Metal Oxides. *Phys. Rev. B: Condens. Matter Mater. Phys.* **2004**, *69*, 235103.

(47) Midgley, P. A.; Weyland, M. 3D Electron Microscopy in the Physical Sciences: The Development of Z-Contrast and EFTEM Tomography. *Ultramicroscopy* **2003**, *96*, 413−431.

(48) Jian, N.; Dowle, M.; Horniblow, R. D.; Tselepis, C.; Palmer, R. E. Morphology of the Ferritin Iron Core by Aberration Corrected Scanning Transmission Electron Microscopy. *Nanotechnology* **2016**, *27* (46), 46LT02.

(49) Pan, Y. H.; Sader, K.; Powell, J. J.; Bleloch, A.; Gass, M.; Trinick, J.; Warley, A.; Li, A.; Brydson, R.; Brown, A. 3D Morphology of the Human Hepatic Ferritin Mineral Core: New Evidence for a Subunit Structure Revealed by Single Particle Analysis of HAADF-STEM Images. *J. Struct. Biol.* **2009**, *166* (1), 22−31.

(50) Stühn, L.; Auernhammer, J.; Dietz, C. PH-Depended Protein Shell Dis- and Reassembly of Ferritin Nanoparticles Revealed by Atomic Force Microscopy. *Sci. Rep.* **2019**, *9* (1), 1−9.

(51) Krisanova, N.; Sivko, R.; Kasatkina, L.; Borysov, A.; Borisova, T. Excitotoxic Potential of Exogenous Ferritin and Apoferritin: Changes in Ambient Level of Glutamate and Synaptic Vesicle Acidification in Brain Nerve Terminals. *Mol. Cell. Neurosci.* **2014**, *58*, 95−104.

(52) Snow, C. L.; Martineau, L. N.; Hilton, R. J.; Brown, S.; Farrer, J.; Boerio-Goates, J.; Woodfield, B. F.; Watt, R. K. Ferritin Iron Mineralization Proceeds by Different Mechanisms in MOPS and Imidazole Buffers. *J. Inorg. Biochem.* **2011**, *105* (7), 972−977.

(53) Xu, B.; Chasteen, N. Iron Oxidation Chemistry in Ferritin. *J. Biol. Chem.* **1991**, *266* (1991), 19965−19970.

(54) Hanna, P. M.; Chen, Y.; Chasteen, N. D. Initial Iron Oxidation in Horse Spleen Apoferritin. Characterization of a Mixed-Valence Iron(II)-Iron(III) Complex. *J. Biol. Chem.* **1991**, *266* (2), 886−893.

(55) Macara, I. G.; Hoy, T. G.; Harrison, P. M. The Formation of Ferritin from Apoferritin. Kinetics and Mechanism of Iron Untake. *Biochem. J.* **1972**, *126*, 151−162.

(56) Yang, X.; Chasteen, N. D. Ferroxidase Activity of Ferritin: Effects of PH, Buffer and Fe(II) and Fe(III) Concentrations on Fe(II) Autoxidation and Ferroxidation. *Biochem. J.* **1999**, *338* (3), 615−618.

(57) Cheng, Y. G.; Chasteen, N. D. Role of Phosphate in Initial Iron Deposition in Apoferritin. *Biochemistry* **1991**, *30* (11), 2947−2953.

(58) Wade, V. J.; Levi, S.; Arosio, P.; Treffry, A.; Harrison, P. M.; Mann, S. Influence of Site-Directed Modifications on the Formation of Iron Cores in Ferritin. *J. Mol. Biol.* **1991**, *221* (4), 1443−1452.

(59) Mehlenbacher, M.; Poli, M.; Arosio, P.; Santambrogio, P.; Levi, S.; Chasteen, N. D.; Bou-Abdallah, F. Iron Oxidation and Core Formation in Recombinant Heteropolymeric Human Ferritins. *Biochemistry* **2017**, *56* (30), 3900−3912.

(60) Pan, Y.-H.; Brown, A.; Sader, K.; Brydson, R.; Gass, M.; Bleloch, A. Quantification of Absolute Iron Content in Mineral Cores of Cytosolic Ferritin Molecules in Human Liver. *Mater. Sci. Technol.* **2008**, *24* (6), 689−694.

(61) Treffry, A.; Bauminger, E. R.; Hechel, D.; Hodson, N. W.; Nowik, I.; Yewdall, S. J.; Harrison, P. M. Defining the Roles of the Threefold Channels in Iron Uptake, Iron Oxidation and Iron-Core Formation in Ferritin: A Study Aided by Site-Directed Mutagenesis. *Biochem. J.* **1993**, *296* (3), 721−728.

(62) Moënne-Loccoz, P.; Krebs, C.; Herlihy, K.; Edmondson, D. E.; Theil, E. C.; Huynh, B. H.; Loehr, T. M. The Ferroxidase Reaction of Ferritin Reveals a Diferric $\mu$-1,2 Bridging Peroxide Intermediate in Common with Other O2-Activating Non-Heme Diiron Proteins. *Biochemistry* **1999**, *38* (17), 5290−5295.

(63) Theil, E. C. Ferritin: The Protein Nanocage and Iron Biomineral in Health and in Disease. *Inorg. Chem.* **2013**, *52*, 12223−12233.

(64) Sparrow, T.G.; Williams, B.G.; Rao, C.N.R.; Thomas, J.M. L3/L2 White Line Intensity Ratios in the Electron Energy- Loss Spectra of 3d Transition Metal Oxides. *Chem. Phys. Lett.* **1984**, *108* (6), 547−550.

(65) Chasteen, N. D.; Harrison, P. M. Mineralization in Ferritin: An Efficient Means of Iron Storage. *J. Struct. Biol.* **1999**, *126* (3), 182−194.

(66) Quintana, C.; Cowley, J. M.; Marhic, C. Electron Nanodiffraction and High-Resolution Electron Microscopy Studies of the Structure and Composition of Physiological and Pathological Ferritin. *J. Struct. Biol.* **2004**, *147* (2), 166−178.

(67) Quintana, C.; Lancin, M.; Marhic, C.; Pérez, M.; Martin-Benito, J.; Avila, J.; Carrascosa, J. L. Initial Studies with High Resolution TEM and Electron Energy Loss Spectroscopy Studies of Ferritin Cores Extracted from Brains of Patients with Progressive Supranuclear Palsy and Alzheimer Disease. *Cell. Mol. Biol.* **2000**, *46* (4), 807−820.

(68) Quintana, C.; Bellefqih, S.; Laval, J. Y.; Guerquin-Kern, J. L.; Wu, T. D.; Avila, J.; Ferrer, I.; Arranz, R.; Patiño, C. Study of the Localization of Iron, Ferritin, and Hemosiderin in Alzheimer's Disease Hippocampus by Analytical Microscopy at the Subcellular Level. *J. Struct. Biol.* **2006**, *153* (1), 42−54.

(69) Galvez, N.; Fernandez, B.; Sanchez, P.; Cuesta, R.; Ceolin, M.; Clemente-Leon, M.; Trasobares, S.; Lopez-Haro, M.; Calvino, J. J.; Stephan, O.; Dominguez-Vera, J. M. Comparative Structural and Chemical Studies of Ferritin Cores with Gradual Removal of Their Iron Contents. *J. Am. Chem. Soc.* **2008**, *130* (25), 8062−8068.

(70) Massover, W. H. Ultrastructure of Ferritin and Apoferritin: A Review. *Micron* **1993**, *24* (4), 389−437.

(71) Pan, Y. H.; Vaughan, G.; Brydson, R.; Bleloch, A.; Gass, M.; Sader, K.; Brown, A. Electron-Beam-Induced Reduction of Fe3+ in Iron Phosphate Dihydrate, Ferrihydrite, Haemosiderin and Ferritin as Revealed by Electron Energy-Loss Spectroscopy. *Ultramicroscopy* **2010**, *110* (8), 1020−1032.

(72) Pan, Y.; Brown, A.; Brydson, R.; Warley, A.; Li, A.; Powell, J. Electron Beam Damage Studies of Synthetic 6-Line Ferrihydrite and Ferritin Molecule Cores within a Human Liver Biopsy. *Micron* **2006**, *37* (5), 403−411.

(73) Moser, T. H.; Mehta, H.; Park, C.; Kelly, R. T.; Shokuhfar, T.; Evans, J. E. The Role of Electron Irradiation History in Liquid Cell Transmission Electron Microscopy. *Sci. Adv.* **2018**, *4*, eaaq1202.

(74) Hart, J. L.; Lang, A. C.; Leff, A. C.; Longo, P.; Trevor, C.; Twesten, R. D.; Taheri, M. L. Direct Detection Electron Energy-Loss Spectroscopy: A Method to Push the Limits of Resolution and Sensitivity. *Sci. Rep.* **2017**, DOI: 10.1038/s41598-017-07709-4.